

PAPER • OPEN ACCESS

# Development of a low-dose strategy for propagation-based imaging helical computed tomography (PBI-HCT): high image quality and reduced radiation dose

To cite this article: Xiaoman Duan *et al* 2025 *Biomed. Phys. Eng. Express* **11** 015049

View the [article online](#) for updates and enhancements.

## You may also like

- [In Situ Formed Phosphoric Acid/Phosphosilicate Nanoclusters in the Exceptional Enhancement of Durability of Polybenzimidazole Membrane Fuel Cells at Elevated High Temperatures](#)  
Jin Zhang, David Aili, John Bradley et al.
- [Near-Infrared-Light Triggered Electron Transfer from Ag<sub>2</sub>S Nanocrystals to Perylene Bisimide](#)  
Yuki Nagai, Tadashi Watanabe, Daisuke Yoshioka et al.
- [Polybenzimidazole \(PBI\) Functionalized Nanographene as Highly Stable Catalyst Support for Polymer Electrolyte Membrane Fuel Cells \(PEMFCs\)](#)  
Le Xin, Fan Yang, Yang Qiu et al.

## Biomedical Physics &amp; Engineering Express



## PAPER

## OPEN ACCESS

RECEIVED  
15 July 2024REVISED  
10 December 2024ACCEPTED FOR PUBLICATION  
16 December 2024PUBLISHED  
26 December 2024

Original content from this work may be used under the terms of the [Creative Commons Attribution 4.0 licence](#).

Any further distribution of this work must maintain attribution to the author(s) and the title of the work, journal citation and DOI.



## Development of a low-dose strategy for propagation-based imaging helical computed tomography (PBI-HCT): high image quality and reduced radiation dose

Xiaoman Duan<sup>1</sup> , Xiao Fan Ding<sup>1</sup> , Samira Khoz<sup>2</sup>, Xiongbiao Chen<sup>1,2</sup> and Ning Zhu<sup>1,3,4</sup> <sup>1</sup> Division of Biomedical Engineering, College of Engineering, University of Saskatchewan, Saskatoon, SK S7N 5A9, Canada<sup>2</sup> Department of Mechanical Engineering, College of Engineering, University of Saskatchewan, Saskatoon, SK S7N 5A9, Canada<sup>3</sup> Department of Chemical and Biological Engineering, College of Engineering, University of Saskatchewan, Saskatoon, SK S7N 5A9, Canada<sup>4</sup> Canadian Light Source, Saskatoon, S7N 2V3, SK, CanadaE-mail: [xbc719@usask.ca](mailto:xbc719@usask.ca) and [niz504@mail.usask.ca](mailto:niz504@mail.usask.ca)**Keywords:** propagation-based imaging computed tomography, radiation dose, convolutional neural network

## Abstract

**Background.** Propagation-based imaging computed tomography (PBI-CT) has been recently emerging for visualizing low-density materials due to its excellent image contrast and high resolution. Based on this, PBI-CT with a helical acquisition mode (PBI-HCT) offers superior imaging quality (e.g., fewer ring artifacts) and dose uniformity, making it ideal for biomedical imaging applications. However, the excessive radiation dose associated with high-resolution PBI-HCT may potentially harm objects or hosts being imaged, especially in live animal imaging, raising a great need to reduce radiation dose. **Methods.** In this study, we strategically integrated Sparse2Noise (a deep learning approach) with PBI-HCT imaging to reduce radiation dose without compromising image quality. Sparse2Noise uses paired low-dose noisy images with different photon fluxes and projection numbers for high-quality reconstruction via a convolutional neural network (CNN). Then, we examined the imaging quality and radiation dose of PBI-HCT imaging using Sparse2Noise, as compared to when Sparse2Noise was used in low-dose PBI-CT imaging (circular scanning mode). Furthermore, we conducted a comparison study on the use of Sparse2Noise versus two other state-of-the-art low-dose imaging algorithms (i.e., Noise2Noise and Noise2Inverse) for imaging low-density materials using PBI-HCT at equivalent dose levels. **Results.** Sparse2Noise allowed for a 90% dose reduction in PBI-HCT imaging while maintaining high image quality. As compared to PBI-CT imaging, the use of Sparse2Noise in PBI-HCT imaging shows more effective by reducing additional radiation dose (30%–36%). Furthermore, helical scanning mode also enhances the performance of existing low-dose algorithms (Noise2Noise and Noise2Inverse); nevertheless, Sparse2Noise shows significantly higher signal-to-noise ratio (SNR) value compared to Noise2Noise and Noise2Inverse at the same radiation dose level. **Conclusions and significance.** Our proposed low-dose imaging strategy Sparse2Noise can be effectively applied to PBI-HCT imaging technique and requires lower dose for acceptable quality imaging. This would represent a significant advance imaging for low-density materials imaging and for future live animals imaging applications.

## 1. Introduction

Propagation-based imaging computed tomography (PBI-CT) is a non-destructive imaging tool that generates high-resolution three-dimensional (3D) digital images of internal object structures (Zeller-Plumhoff *et al* 2017, Preissner *et al* 2018, Taba *et al* 2019, Tavakoli Taba *et al* 2020, Duan *et al* 2021, Albers *et al* 2023). PBI-

CT utilizes absorption and refraction information, offering superior image contrast for low-density objects. Compared with conventional circular PBI-CT scanning mode, PBI-CT with a helical acquisition mode (PBI-HCT) (Pelt and Parkinson 2018, Duan *et al* 2023b) shows the more advanced imaging advantages due to its capability to address ring artifacts and enhance image quality, and achieve uniform dose distribution

(Duan *et al* 2023b), thereby highly suitable for biomedical imaging applications. Though promising, the associated high radiation dose in PBI-HCT may potentially harm scanned objects or hosts. The recent work revealed that the radiation dose of PBI-HCT was closely associated to the parameter of *pitch*, defined as the ratio of vertical distance travelled per rotation to the height of the active detector for each single slice (unitless) (Duan *et al* 2023b). Given that *pitch* is usually smaller than 2 in parallel x-ray beam imaging to prevent information loss, the radiation dose of PBI-HCT is even higher than that of PBI-CT imaging. This raises a great need to develop the low-dose imaging strategies for PBI-HCT, particularly for biomedical imaging.

In recent years, computational algorithms, especially deep learning (DL) (Chen *et al* 2017, Kang *et al* 2017, Shan *et al* 2019, Wang *et al* 2020) based algorithms, become more popular which have been proven effective to low-dose CT imaging which can accurately denoise and/or remove artifacts in the reconstruction of low-dose images while maintaining high image quality. However, no specialized computational algorithms have been reported for low-dose PBI-HCT imaging.

In this work, we developed an innovative algorithm called Sparse2Noise which can effectively improve the image quality for low-dose PBI-HCT imaging. Sparse2Noise achieves high-quality image by using paired sets of low-dose noisy images acquired under different photon fluxes and with varying numbers of projections. These paired image sets are used as input (normal-flux sparse-view) and target (low-flux full-view) data for training a convolutional neural network (CNN). Sparse2Noise does not rely on high-quality reconstructed data obtained from high radiation doses as references, making it highly applicable for practical scenarios. The previous work (Duan *et al* 2023a) has demonstrated the outstanding performance of Sparse2Noise for low-dose PBI-CT imaging to maintain high image quality. Therefore, this study primarily evaluated the performance of Sparse2Noise when applied to PBI-HCT imaging and compared to the performance when Sparse2Noise applied to PBI-CT at same radiation dose level. More significantly, benefiting from the advantage of removing ring artifacts in PBI-HCT, it is possible to relax the input requirements of Sparse2Noise from a normal-flux sparse-view scan to a low-flux sparse-view scan when Sparse2Noise is applied to PBI-HCT imaging. By adopting this strategy, the evident advantage is a further reduction in radiation dose, which is always preferred for biomedical imaging applications.

Additionally, Noise2Noise (Lehtinen *et al* 2018, Wu *et al* 2019, Hasan *et al* 2020, Yuan *et al* 2020) and Noise2Inverse (Hendriksen *et al* 2020) are two state-of-the-art DL-based denoising algorithms that hold potential for low-dose PBI-HCT imaging. These methods are self-supervised and do not require clean images as training targets. Noise2Noise utilizes paired

sets of low-dose noisy images as inputs and targets for the CNN model, producing high-quality results as the training progresses. In contrast, Noise2Inverse uses a single set of low-dose CT scans and divides the noisy projections into different complementary datasets, which are then used to reconstruct the CT images as inputs and targets for the CNN model. The recent work (Duan *et al* 2023a) has shown that Noise2Noise and Noise2Inverse algorithms can be used for low-dose PBI-CT imaging but they faced challenges in producing satisfactory results. One of the reasons for this limitation arises from the severe ring artifacts exhibited in both the input data and target data, particularly in the context of extremely low-dose imaging. However, when these algorithms are applied to PBI-HCT, the ring artifacts can be pre-emptively removed, which has the potential to enhance the performance of these algorithms in low-dose imaging scenarios. Consequently, the performances of these two algorithms for low-dose PBI-HCT imaging were evaluated. Finally, a comprehensive analysis on the image quality obtained through Sparse2Noise, Noise2Noise, and Noise2Inverse algorithms was compared at the same radiation doses.

This paper presents our novel study on low-dose PBI-HCT imaging using Sparse2Noise. The Materials and Methods section begins by outlining the theoretical framework of Sparse2Noise when utilized for low-dose PBI-HCT imaging. Following this, the section presents our experimental studies aimed at assessing the feasibility of various algorithms for low-dose PBI-HCT imaging, compared with PBI-CT imaging for different samples at the same dose level. Two kinds of samples, i.e., low-density hydrogel tissue scaffold sample and rat's hindlimb sample with scaffolds implanted (help in the regeneration of injured nerves) and were used for evaluating the performance of proposed strategy. Subsequently, we present the results and discussion regarding related, yet significant, issues and interpretations, concluding with insights gleaned from the present work. Finally, a brief conclusion is provided.

## 2. Materials and methods

### 2.1. Theoretical framework of Sparse2Noise for PBI-HCT imaging

Let  $\mathbf{y}^*$ ,  $\mathbf{y}$ , and  $\tilde{\mathbf{y}}$  be the clean, normal-flux and low-flux image (i.e., sinogram) collected in transmission measurement domain of PBI-CT imaging, respectively. The relationship between these three variables can be represented as:

$$\tilde{\mathbf{y}} = \mathbf{y} + \epsilon = \mathbf{y}^* + \mathbf{y}^* \odot \eta_p + \epsilon, \quad (1)$$

where  $\mathbf{y}^* \odot \eta_p$  ( $\odot$  is element-wise multiplication) is modelled as an angular correlation noise and  $\epsilon$  denotes i.i.d. mean-zero noise (i.e., low-flux noise). The angular streak/stripe noise  $\eta_p$  on normal-flux

image and low-flux image are hypothesized to be independent to each other.

In the measurement domain, the difference between PBI-HCT and PBI-CT reconstruction lies on the virtual sinogram conversion (Duan *et al* 2023b), which can be represented with a linear offset relationship represented by the constant matrix  $\mathbf{K}$ . As a result, the virtual converted sinogram in PBI-HCT imaging,  $\mathbf{y}^* \rightarrow \mathbf{K}\mathbf{y}^*$ ,  $\mathbf{y} \rightarrow \mathbf{K}\mathbf{y}$ , and  $\tilde{\mathbf{y}} \rightarrow \mathbf{K}\tilde{\mathbf{y}}$ .

According to CT reconstruction algorithm, i.e., filtered back-projection algorithm (FBP), the reconstruction  $\mathbf{x}$  and  $\tilde{\mathbf{x}}$  can be obtained from the measured data  $\mathbf{y}$  and  $\tilde{\mathbf{y}}$  with linear reconstruction operator  $\mathbf{R}$ ,

$$\mathbf{x} = \mathbf{R}\mathbf{K}\mathbf{y} = \mathbf{R}\mathbf{K}(\mathbf{y}^* + \mathbf{y}^* \odot \eta_p), \quad (2)$$

$$\begin{aligned} \tilde{\mathbf{x}} &= \mathbf{R}\mathbf{K}\tilde{\mathbf{y}} = \mathbf{R}\mathbf{K}(\mathbf{y}^* + \mathbf{y}^* \odot \eta_p + \epsilon) \\ &= \mathbf{x}^* + \mathbf{R}\mathbf{K}(\mathbf{y}^* \odot \eta_p) + \mathbf{R}\mathbf{K}\epsilon. \end{aligned} \quad (3)$$

The training task of Sparse2Noise based on CNN for low-dose PBI-HCT imaging is to determine the parameters that best enable the network  $f_\varphi$ ,

$$\hat{\varphi} = \arg \min_{\varphi} \|f_\varphi(\mathbf{x}^S) - \tilde{\mathbf{x}}^F\|_2^2, \quad (4)$$

where  $\mathbf{x}^S$  is the normal-flux sparse-view (i.e., sparse projections are acquired with uniform under-sampling) reconstruction and  $\tilde{\mathbf{x}}^F$  is the low-flux full-view reconstruction. We denote with  $\mu$  the joint measure of  $\mathbf{x}$ ,  $\eta_p$ , and  $\epsilon$ . In this case, the trained network  $f_\varphi$  obtained in equation (4) approximates the regression function,

$$h^* = \arg \min_h \mathbb{E}_\mu \|h(\mathbf{x}^S) - \tilde{\mathbf{x}}^F\|^2. \quad (5)$$

We introduce  $\mathbf{x}^{*F}$  in equation (5) and expand the squared norm,

$$\begin{aligned} \|h(\mathbf{x}^S) - \tilde{\mathbf{x}}^F\|^2 &= \|h(\mathbf{x}^S) - \mathbf{x}^{*F} + \mathbf{x}^{*F} - \tilde{\mathbf{x}}^F\|^2 \\ &= \|h(\mathbf{x}^S) - \mathbf{x}^{*F}\|^2 + \|\mathbf{x}^{*F} - \tilde{\mathbf{x}}^F\|^2 \\ &\quad + 2[h(\mathbf{x}^S) - \mathbf{x}^{*F}]^T [\mathbf{x}^{*F} - \tilde{\mathbf{x}}^F]. \end{aligned} \quad (6)$$

The expectation of the third term is,

$$\begin{aligned} &\mathbb{E}_\mu [h(\mathbf{x}^S) - \mathbf{x}^{*F}]^T [\mathbf{x}^{*F} - \tilde{\mathbf{x}}^F] \\ &= \mathbb{E}_\mu [h(\mathbf{x}^S)^T \mathbf{x}^{*F} - \mathbf{x}^{*FT} \mathbf{x}^{*F} - h(\mathbf{x}^S)^T \tilde{\mathbf{x}}^F + \mathbf{x}^{*FT} \tilde{\mathbf{x}}^F]. \end{aligned} \quad (7)$$

Let's focus on the third term,

$$\begin{aligned} \mathbb{E}_\mu [h(\mathbf{x}^S)^T \tilde{\mathbf{x}}^F] &= \mathbb{E}_\mu [h(\mathbf{x}^S)^T (\mathbf{x}^{*F} + \mathbf{R}_F \mathbf{K}(\mathbf{y}_F^* \odot \eta_p) + \mathbf{R}_F \mathbf{K}\epsilon)] \\ &= \mathbb{E}_\mu [h(\mathbf{x}^S)^T \mathbf{x}^{*F} + h(\mathbf{x}^S)^T \mathbf{R}_F \mathbf{K}(\mathbf{y}_F^* \odot \eta_p) + h(\mathbf{x}^S)^T \mathbf{R}_F \mathbf{K}\epsilon], \end{aligned} \quad (8)$$

$\eta_p$  and  $\epsilon$  are both mean-zero and independent for normal-flux and low-flux scan and  $\mathbf{y}_F^*$  is a constant variable free of random noise, therefore,

$$\begin{aligned} &\mathbb{E}_\mu [h(\mathbf{x}^S)^T \mathbf{R}_F \mathbf{K}(\mathbf{y}_F^* \odot \eta_p) + h(\mathbf{x}^S)^T \mathbf{R}_F \mathbf{K}\epsilon] \\ &= \mathbb{E}_\mu [h(\mathbf{x}^S)^T \mathbf{R}_F \mathbf{K} \mathbb{E}_\mu (\mathbf{y}_F^* \odot \eta_p) + 0] = 0. \end{aligned} \quad (9)$$

As a result, equation (8) can be simplified as,

$$\mathbb{E}_\mu [h(\mathbf{x}^S)^T \tilde{\mathbf{x}}^F] = \mathbb{E}_\mu [h(\mathbf{x}^S)^T \mathbf{x}^{*F}]. \quad (10)$$

Likewise, we have,

$$\mathbb{E}_\mu [\mathbf{x}^{*FT} \tilde{\mathbf{x}}^F] = \mathbb{E}_\mu [\mathbf{x}^{*FT} \mathbf{x}^{*F}]. \quad (11)$$

Then equation (7) yields,

$$\mathbb{E}_\mu [h(\mathbf{x}^S) - \mathbf{x}^{*F}]^T [\mathbf{x}^{*F} - \tilde{\mathbf{x}}^F] = 0. \quad (12)$$

Finally, we can obtain the expected prediction error decomposition in equation (6) as,

$$\begin{aligned} \mathbb{E}_\mu \|h(\mathbf{x}^S) - \tilde{\mathbf{x}}^F\|^2 &= \mathbb{E}_\mu \|h(\mathbf{x}^S) - \mathbf{x}^{*F}\|^2 \\ &\quad + \mathbb{E}_\mu \|\mathbf{x}^{*F} - \tilde{\mathbf{x}}^F\|^2. \end{aligned} \quad (13)$$

This equation demonstrates that the expected prediction error can be decomposed into the supervised prediction error and the variance of the noise error in the low-flux full-view reconstruction. By training a CNN, Sparse2Noise can be applied in PBI-HCT to yield the full-view clean reconstruction  $\mathbf{x}^{*F}$ .

## 2.2. Experimental samples preparation

In this work, we used hydrogel tissue scaffolds as the imaging low-density samples. Hydrogel scaffolds made from biomaterials (e.g., alginate, gelatin, chitosan) are used to support and facilitate the injured tissue regeneration, and therefore are essential to tissue engineering and regenerative medicine applications (Mohabtpour *et al* 2022, Chen *et al* 2023). Visualization and characterization of scaffolds before and after implantation into the host is essential to evaluate the regeneration of injured tissues. As a non-destructive imaging method, PBI-CT is able to offer high resolution and superior image contrast for low-density objects compared to conventional imaging methods, thereby being suitable for the visualization and characterization of tissue scaffolds (Ning *et al* 2021).

### 2.2.1. Hydrogel scaffold samples

4% weight/volume (w/v) aqueous alginate made from medium-viscosity alginate powder (alginic acid sodium salt from brown algae, CAS 9005-38-3, Sigma-Aldrich) was prepared to be scanned with PBI-HCT imaging. The scaffold fabrication process was similar to the procedure developed in a previous study (Ning *et al* 2021). Scaffolds were fabricated with the dimensions of  $10 \times 10 \times 5$  mm with a strand diameter of 500  $\mu\text{m}$  following a grid pattern (figure 1(A)).

### 2.2.2. Rat's hindlimb with scaffolds implanted

In addition to imaging the hydrogel scaffold itself before implantation, we also scanned the scaffolds after implantation into the animals. The scaffolds were constructed with dimensions of  $2 \times 10 \times 2$  mm for rat's sciatic nerve regeneration and a strand diameter of 500  $\mu\text{m}$ , adhering to a grid pattern (figure 1(B)). Two male adult Sprague-Dawley's rats were procured from Charles River Company for this study. A transection of the sciatic nerve served as the model for the scaffold implantation experiments. This animal study

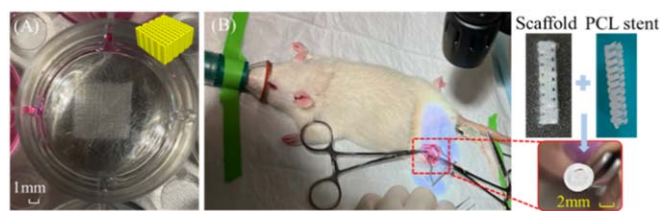


**Figure 1.** Samples for PBI-HCT imaging. (A) A printed hydrogel tissue scaffold and (B) a printed hydrogel scaffold encased in a PCL stent and subsequently implanted in a rat's hindlimb for sciatic nerve regeneration.

was approved by the Canadian Council on Animal Care (CCAC), University Animal Care Committee's Animal Research Ethics Board at the University of Saskatchewan - approval: 20220094.

The hydrogel scaffold, enclosed in a polycaprolactone (PCL) spiral stent, was then implanted into the transected nerve. Two days post-surgery, the rat was terminally anesthetized with isoflurane. Subsequently, euthanasia was performed through transcardial perfusion with PBS, followed by a fixative solution. The entire left hindlimb, including the scaffolds, was disarticulated and placed in 50 ml centrifuge tubes with formalin solution, which were scanned using PBI-HCT.

### 2.3. PBI-HCT imaging

The PBI-HCT imaging experiments were performed at the 05ID-2 beamline (Wysokinski *et al* 2007, Gasilov *et al* 2024), at the Canadian Light Source (CLS). In our experiments, the projections were acquired using a monochromatic energy of 30 keV and a propagation distance of 1.5 m, both of which were shown to provide the best image quality for hydrogel tissue scaffold imaging in our previous study (Duan *et al* 2023b). The adjustment of photon flux can be achieved using the Lucite neutral density filters (NDF) with different thickness. The key feature of NDF is that they reduce the number of photons across all energies in the spectrum uniformly, meaning the overall energy distribution of the photons (i.e., the spectrum) remains unchanged. The indirect detection setup, with an effective pixel size of 13  $\mu\text{m}$  and an image depth of 16-bit, consisted of beam monitor (AA60 HAMAMATSU, Japan) with a scintillator (LuAg500, Lutetium  $\text{Lu}_3\text{Al}_5\text{O}_{12}$  garnet (LuAG) doped by the luminescent  $\text{Ce}^{3+}$ , thickness of 500  $\mu\text{m}$ ) converting x-rays to visible light, an optic system, and a scientific metal-oxide-semiconductor (sCMOS) digital camera (ORCA Flash 4.0). The active areas of the detector for PBI-CT and for PBI-HCT imaging were 9.3 mm  $\times$  26.6 mm and 2.6 mm  $\times$  26.6 mm, respectively. The exposure time was set at 30 ms per projection.

#### 2.3.1. Sparse2Noise for low-dose PBI-HCT imaging

Table 1 gives the specific experimental parameters and corresponding measured dose (details of the measurement can be found in our previous work (Duan *et al*

2023b)) of eight different low-dose PBI-HCT data using Sparse2Noise. Specifically,

- Group #1 (Data #1 and Data #2) was intended to assess the performance of Sparse2Noise for PBI-HCT and PBI-CT on hydrogel tissue scaffold sample with binning 1  $\times$  1 (pixel size of 13  $\mu\text{m}$ ), while Group #2 (Data #3 and Data #4) pertains to rat's hindlimb samples with scaffolds implanted with binning 2  $\times$  2 mode (pixel size of 26  $\mu\text{m}$ ).
- Group #3 (Data #5 and Data #6) was designed to evaluate the performance of Sparse2Noise with relaxed requirements. In this setup, the input data consisted of low-flux sparse-view scans with a reduced photon flux (72% reduction in photon number), achieved by utilizing a NDF of 40 mm, in contrast to the conventional normal-flux sparse-view scans with a NDF of 0 mm. This evaluation encompassed both low-dose PBI-HCT and PBI-CT imaging of hydrogel tissue scaffold sample. Likewise, Group #4 (Data #7 and Data #8) pertained to rat's hindlimb sample with scaffolds implanted.

PBI-HCT images exhibit edge enhanced intensity information induced by phase shift, yet they do not depict phase shift value (Zhang *et al* 2021). Phase retrieval emerges as an advanced technique capable of extracting phase shift value for PBI-HCT imaging from the intensity measurements obtained during sample scans (Zhang *et al* 2021). From image processing aspect, this technique converts the edge contrast to area contrast, thereby enhancing contrast-to-noise ratio (CNR) in images and conducting quantitative analysis like segmentation, especially for low-density materials in biomedical imaging applications.

After collecting the paired PBI-HCT data for Sparse2Noise, flat-dark correction and phase retrieval (i.e., transport of intensity equation, TIE or Paganin algorithm with  $\delta/\beta = 1000$ ) (Paganin *et al* 2002) were applied. We selected a  $\delta/\beta$  of 1000 based on empirical data, as the hydrogel tissue scaffolds are low-density materials similar to biological tissues and other soft materials. For imaging biological tissues and soft materials at an x-ray energy of 30 keV, a  $\delta/\beta$  value of 1000 is commonly used (Momose 2020) for sufficient contrast. For PBI-HCT data, the sinogram were converted to virtual PBI-CT data following the procedure



**Table 1.** Details of the experimental conditions for PBI-HCT and PBI-CT imaging, pertaining to *eight* different datasets utilized for Sparse2Noise.

Group	Data	Input and target	Scanning mode	Sample	Binning	NDF (mm)	$Np$	Dose (Gy)
#1	1	Normal-flux sparse-view	PBI-CT	Hydrogel tissue scaffolds	$1 \times 1$	0	62	1.8
		Low-flux full-view	PBI-CT			80	900	1.8
	2	Normal-flux sparse-view	PBI-HCT <sup>a</sup>	Hydrogel tissue scaffolds	$1 \times 1$	0	62	1.8
		Low-flux full-view	PBI-HCT			80	900	1.8
#2	3	Normal-flux sparse-view	PBI-CT	Rat's hindlimb with scaffolds implanted	$2 \times 2$	0	68	0.5
		Low-flux full-view	PBI-CT			80	1000	0.5
	4	Normal-flux sparse-view	PBI-HCT	Rat's hindlimb with scaffolds implanted	$2 \times 2$	0	68	0.5
		Low-flux full-view	PBI-HCT			80	1000	0.5
#3	5	Low-flux sparse-view	PBI-CT	Hydrogel tissue scaffolds	$1 \times 1$	40	62	0.5
		Low-flux full-view	PBI-CT			80	900	1.8
	6	Low-flux sparse-view	PBI-HCT	Hydrogel tissue scaffolds	$1 \times 1$	40	62	0.5
		Low-flux full-view	PBI-HCT			80	900	1.8
#4	7	Low-flux sparse-view	PBI-CT	Rat's hindlimb with scaffolds implanted	$2 \times 2$	40	68	0.2
		Low-flux full-view	PBI-CT			80	1000	0.5
	8	Low-flux sparse-view	PBI-HCT	Rat's hindlimb with scaffolds implanted	$2 \times 2$	40	68	0.2
		Low-flux full-view	PBI-HCT			80	1000	0.5

<sup>a</sup> Pitch of 2 was used for all PBI-HCT imaging;  $Np$ : the effective number of projections per  $180^\circ$ .

published in the previous work (Duan *et al* 2023b). Then, FBP reconstruction was realized using *tofu* toolkit (Faragó *et al* 2022) with Ram-Lak filter. In this work, U-Net (Shan *et al* 2018) with three down-sampling layers and three up-sampling layers was used as the network for training Sparse2Noise. The primary modification to the U-Net network involves using a stack of  $d$  adjacent images as the input ( $d \geq 1$ ,  $d = 3$  in this work), followed by the application of eight  $1 \times 1$  convolutional kernels. The loss function for U-Net is L1 loss, which is found to perform well for restoring high-frequency details. U-Net was trained using the ADAM algorithm with a mini-batch size of 64 and a learning rate of  $10^{-4}$ . More details on the optimization and implementation of Sparse2Noise, as well as the ablation studies, can be found in our previous work (Duan *et al* 2023a).

After obtaining the results of Sparse2Noise, in addition to qualitative observation, quantitative analysis in terms of signal-to-noise ratio (SNR) and CNR (Duan *et al* 2023b) were also calculated following,

$$\text{SNR} = \left| \frac{I_{E_{\text{foreground}}}}{\sigma_{\text{background}}} \right|, \quad (14)$$

$$\text{CNR} = \left| \frac{I_{E_{\text{foreground}}} - I_{E_{\text{background}}}}{\sigma_{\text{background}}} \right|. \quad (15)$$

$I_E$  and  $\sigma$  denote the mean grey value and standard deviation of the regions of interest (ROI). Foreground indicates the ROI including objective hydrogel scaffolds while background represents the ROI of air, excluding the sample area.

Besides, we also evaluated other factors such as grey value profile (0–255), spatial resolution (represented by modulation transfer function (MTF) (Samei *et al* 2019), edge spread function (ESF) based), and one-dimensional (1D) noise power spectrum (NPS) (i.e., the radial average profile of the 2D NPS) (Chen *et al* 2014) in our examination by using different algorithms. For calculating NPS, we performed two scans of the same sample under identical imaging conditions. The difference between the two scans produced a noise-dominant image without structural information. We then extracted a  $64 \times 64$  ROI from the center of the noise image and calculated the 2D NPS as below:

$$\text{NPS}_{2D} = \frac{1}{2} \cdot \frac{\Delta x \Delta y}{N_x N_y} \cdot |DFT_{2D} \{I_1(x, y) - I_2(x, y)\}|^2. \quad (16)$$

where  $N_x$  and  $N_y$  denote the number of pixels along the row and column directions within the ROI, and  $\Delta x$  and  $\Delta y$  are the sampling intervals used in the 2D discrete Fourier transform (DFT).

### 2.3.2. Noise2Noise and Noise2Inverse for low-dose PBI-HCT imaging

Noise2Noise utilizes paired low-dose noisy images as the input and target when training the network. For low-dose PBI-HCT (pitch of 2) imaging, the input and

target data are both low-flux (with NDF of 80 mm) full-view imaging. Specifically, for hydrogel tissue scaffolds imaging, the binning mode was  $1 \times 1$  with  $N_p$  of 900 and the dose was 1.8 Gy for both input and target data. For imaging of rat's hindlimb sample with scaffolds implanted, the binning mode was  $2 \times 2$  with  $N_p$  of 1000 and the dose was 0.5 Gy for both input and target data.

Different from Sparse2Noise and Noise2Noise, Noise2Inverse (Hendriksen *et al* 2020) operates on single low-dose noisy imaging datasets but with double number of projections owing to its split principle. This adjustment effectively mitigates under-sampling artifacts. For hydrogel tissue scaffolds imaging, the binning mode was  $1 \times 1$  with  $N_p$  of 1800 and NDF of 80 mm. For imaging of rat's hindlimb sample with scaffolds implanted, the binning mode was  $2 \times 2$  with  $N_p$  of 2000 and NDF of 80 mm. The corresponding total doses were 3.6 Gy for hydrogel tissue scaffolds and 1 Gy for rat's hindlimb sample with scaffolds, respectively.

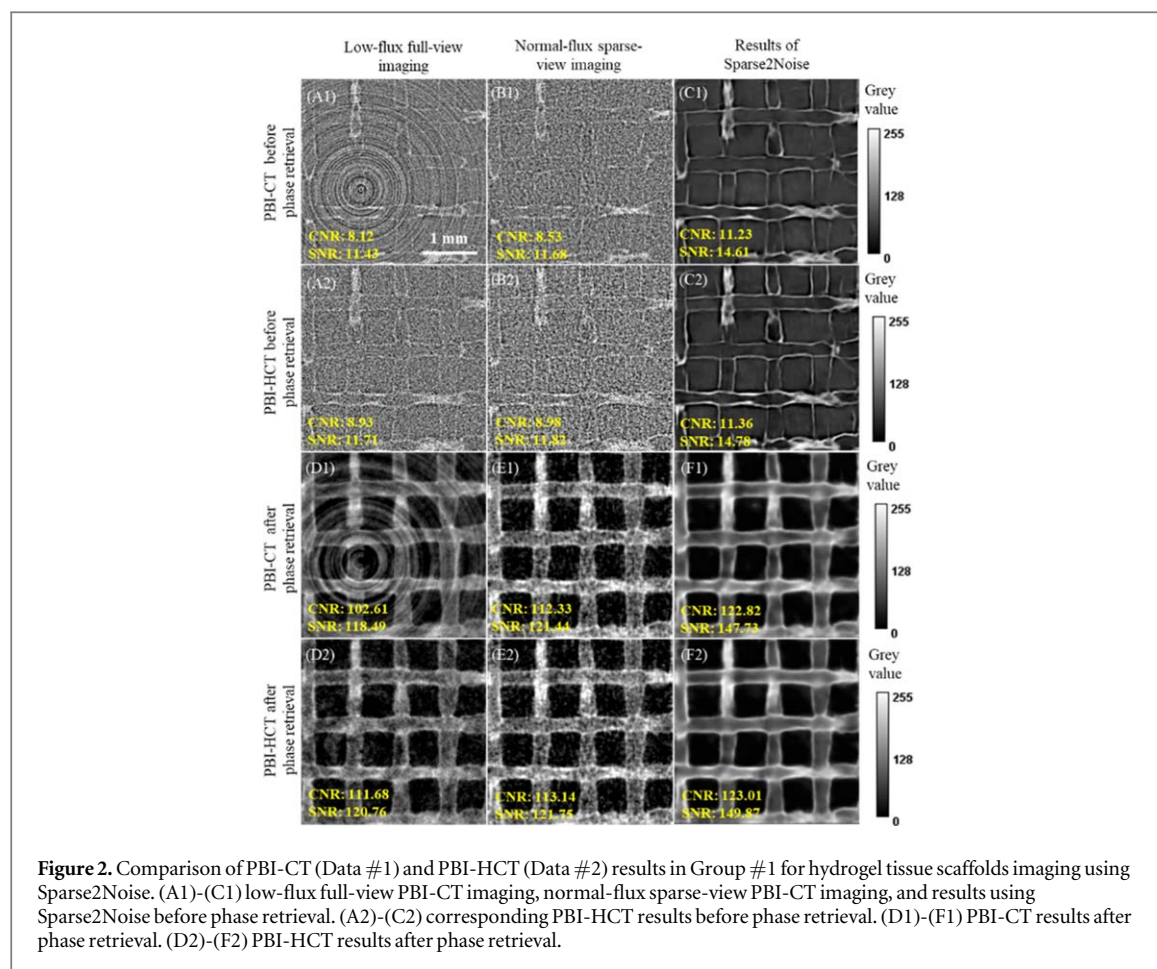
We compared the performance of Noise2Noise and Noise2Inverse for low-dose PBI-CT data processing with their performance when used for low-dose PBI-HCT data processing. The same network architecture, parameters, and training strategy as used in Sparse2Noise were applied for consistency in the comparison.

## 3. Results

### 3.1. Sparse2Noise for low-dose PBI-HCT imaging

Figure 2 presents the results of low-dose PBI-CT and low-dose PBI-HCT imaging for hydrogel tissue scaffolds before and after phase retrieval using Sparse2Noise. Before phase retrieval, the results represent the direct reconstruction of low-dose PBI-CT, which inherently exhibit edge enhancement. These edge-enhanced results effectively highlight clear tissue scaffold boundaries with high resolution, aiding in pinpointing the scaffold positions. After phase retrieval, the edge contrast is converted to area contrast, which is beneficial for subsequent quantitative processing such as segmentation. However, the smoothing effect near boundaries can slightly compromise the accuracy of scaffold position resolution. Therefore, both results before and after phase retrieval offer unique advantages, and should be processed using Sparse2Noise.

From figure 2, first, from the images of low-flux full-view imaging, it becomes evident that utilizing PBI-HCT provides a noticeable enhancement in image quality compared to PBI-CT, particularly in the removal of ring artifacts. Second, it can be observed that the results obtained from PBI-CT and PBI-HCT exhibit similarity for normal-flux sparse-view imaging, where the primary challenge lies in under-sampling artifacts rather than ring artifacts. Third, the



results of PBI-HCT using Sparse2Noise demonstrate substantial improvement in image quality, particularly in terms of noise reduction. Importantly, owing to the inherent capability of Sparse2Noise to remove ring artifacts in addition to denoising, the Sparse2Noise results for PBI-CT and PBI-HCT similar to each other. This demonstrates the effectiveness of Sparse2Noise in achieving comparable results for both scanning modes. Quantitative analysis in terms of SNR and CNR (Duan et al 2023b) for these results also supports our observations, providing detailed metrics to support the effectiveness and similarity of Sparse2Noise in enhancing image quality for both PBI-CT and PBI-HCT imaging scenarios.

Similar conclusion can be obtained for rat's hindlimb sample with scaffolds implanted, as shown in figure 3.

The red arrows indicate the degraded and swollen scaffolds. These results emphasize the importance of using phase retrieval to enhance contrast for visualizing rat's hindlimb sample with scaffolds implanted. Before phase retrieval, low-dose results showed some visibility of the PCL stent, but tissue scaffolds could still not be identified. After phase retrieval, PCL stent and tissue scaffolds are both visible and can be used to characterize the architecture properties (e.g., volume). Besides, low-flux full-view imaging and normal-flux sparse-view imaging suffer from either ring artifacts or

under-sampling artifacts, respectively, making it challenging to accurately characterize the volume of tissue scaffolds. By applying Sparse2Noise, although the precise structure of the tissue scaffolds may still appear somewhat indistinct due to degradation and swelling (resulting in scaffold intensities resembling those of surrounding soft tissues, with only edges being clearly shown), there has been a significant enhancement in image quality. This improvement enables more effective localization of the scaffold volume based on its boundaries.

Figure 4 illustrates the analysis of hydrogel tissue scaffolds using PBI-CT (Data #5) and PBI-HCT (Data #6) before and after phase retrieval of Group #3, utilizing Sparse2Noise with low-flux sparse-view imaging as input (i.e., the relaxed requirements). In comparison to the PBI-CT imaging, the application of Sparse2Noise to PBI-HCT imaging yields superior image quality, producing results that are similar to those achieved with normal-flux sparse-view imaging, as shown in figure 2. This is attributed to the reduction of ring artifacts of input data in PBI-HCT.

While Sparse2Noise exhibits the capability to remove ring artifacts along with denoising, its effectiveness encounters limitations, particularly in cases of extremely low-dose imaging where relatively severe ring artifacts are present in both input and target data. In such scenarios, the assumption that ring artifacts



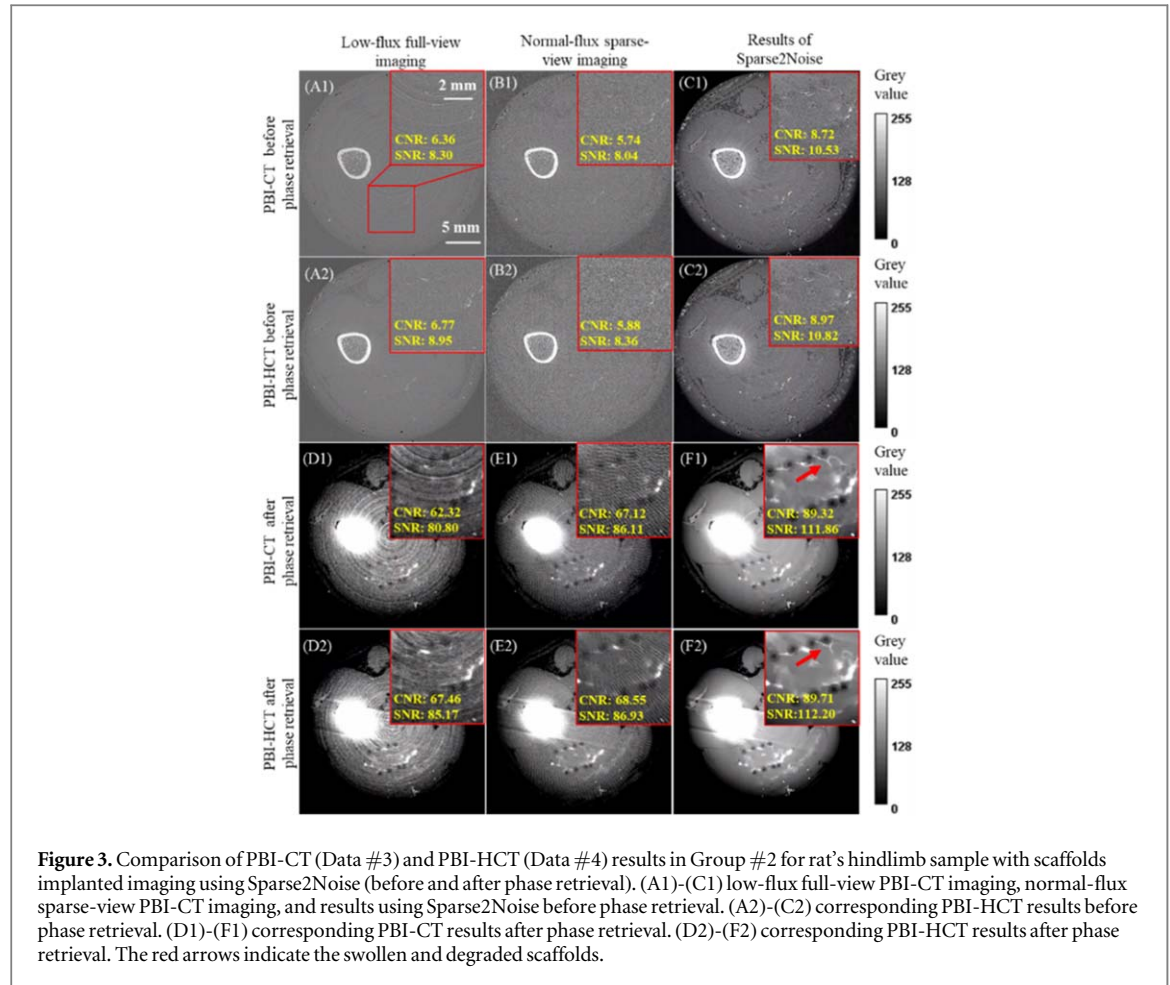


**Figure 3.** Comparison of PBI-CT (Data #3) and PBI-HCT (Data #4) results in Group #2 for rat's hindlimb sample with scaffolds implanted imaging using Sparse2Noise (before and after phase retrieval). (A1)-(C1) low-flux full-view PBI-CT imaging, normal-flux sparse-view PBI-CT imaging, and results using Sparse2Noise before phase retrieval. (A2)-(C2) corresponding PBI-HCT results before phase retrieval. (D1)-(F1) corresponding PBI-CT results after phase retrieval. (D2)-(F2) corresponding PBI-HCT results after phase retrieval. The red arrows indicate the swollen and degraded scaffolds.

are independent of the input and target is no longer valid, leading to residual artifacts in the results. However, when Sparse2Noise is applied to PBI-HCT, the ring artifacts in the input data are removed in advance, ensuring that the results with invisible ring artifacts. As a result, the improvements observed in the results obtained from PBI-HCT compared to PBI-CT are notably more pronounced. This improvement achieved through Sparse2Noise for PBI-HCT facilitates a further reduction in dose by 36% (i.e.,  $100\% \times \left(1 - \frac{(Dose_{input} + Dose_{target})_{PBI-HCT}}{(Dose_{input} + Dose_{target})_{PBI-CT}}\right) = 100\% \times \left(1 - \frac{0.5Gy + 1.8Gy}{1.8Gy + 1.8Gy}\right)$ ) compared to PBI-CT.

Similar conclusion for rat's hindlimb sample with scaffolds implanted results after phase retrieval using Sparse2Noise with low-flux sparse-view imaging as input can be found in figure 5.

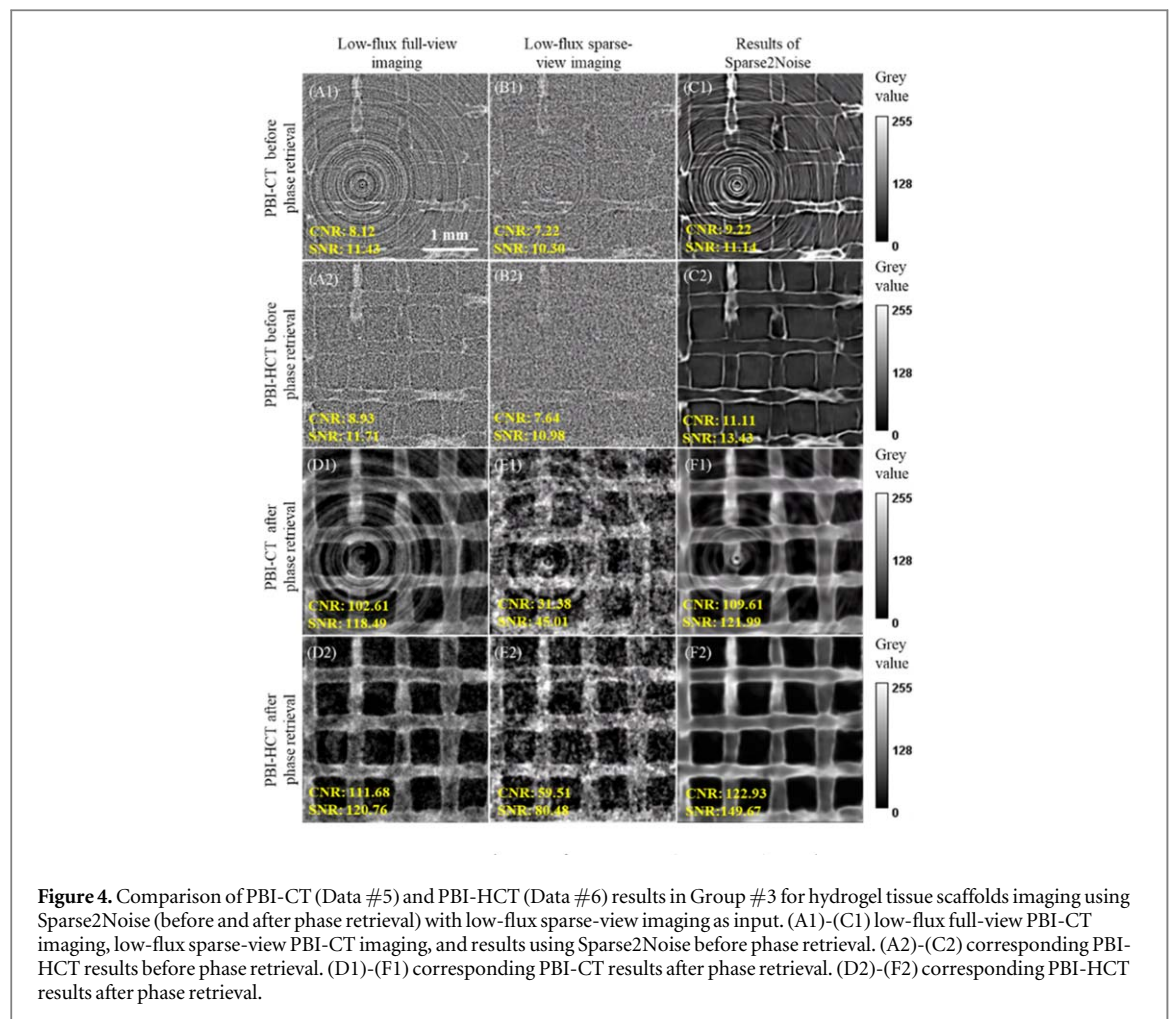
Results before phase retrieval are not displayed due to limited information can be provided. The image quality of PBI-HCT, processed by Sparse2Noise, outperforms that of PBI-CT in terms of removing ring artifacts, while closely resembling the results obtained when employing normal-flux sparse-view imaging as input with Sparse2Noise. The tissue scaffolds and PCL stent are more distinguishable in PBI-HCT images and the images have few ring artifacts compared to PBI-CT images. This improvement achieved

through Sparse2Noise for PBI-HCT facilitates a further reduction in dose by 30% (i.e.,  $100\% \times \left(1 - \frac{(Dose_{input} + Dose_{target})_{PBI-HCT}}{(Dose_{input} + Dose_{target})_{PBI-CT}}\right) = 100\% \times \left(1 - \frac{0.2Gy + 0.5Gy}{0.5Gy + 0.5Gy}\right)$ ) compared to PBI-CT.

### 3.2. Noise2Noise and Noise2Inverse for low-dose PBI-HCT imaging

Figure 6 displays the results of hydrogel tissue scaffolds and rat's hindlimb sample with scaffolds implanted utilizing Noise2Noise. Despite exhibiting some ring artifacts in low-dose PBI-CT images, Noise2Noise demonstrates superior performance in PBI-HCT images, with fewer ring artifacts observed. Hence, in addition to Sparse2Noise, Noise2Noise can be as an alternative low-dose imaging strategy suitable for PBI-HCT applications. Nevertheless, quantitative analysis in terms of SNR and CNR reveals that the image quality obtained using Noise2Noise is slightly lower compared to the results of Sparse2Noise (refer to figures 4 and 5).

Figure 7 presents the results of hydrogel tissue scaffolds and rat's hindlimb sample with scaffolds implanted utilizing Noise2Inverse. In the PBI-CT data, noticeable ring artifacts are evident, severely impacting image quality and disrupting the structures of the tissue scaffold and stent. However, when



Noise2Inverse is applied to PBI-HCT, both before and after phase retrieval, superior image quality is achieved, with fewer observed ring artifacts and relatively discernible tissue scaffold and stent structures. Therefore, in addition to Sparse2Noise and Noise2Noise, Noise2Inverse can also serve as an alternative low-dose imaging strategy suitable for PBI-HCT applications. Nevertheless, quantitative analysis in terms of SNR and CNR reveals that the image quality obtained using Noise2Inverse is slightly lower compared to the results of Sparse2Noise and Noise2Noise.

### 3.3. Quantitative analysis of various algorithms for low-dose PBI-HCT imaging

Figure 8 presents the statistical quantitative analysis of PBI-HCT results using different algorithms, i.e., Sparse2Noise, Noise2Noise, and Noise2Inverse, all acquired at equal doses of 3.6 Gy for hydrogel tissue scaffolds (on 660 PBI-HCT images) and 1 Gy for rat's hindlimb sample with scaffolds implanted (on 450 PBI-HCT images).

While qualitatively, the PBI-HCT results exhibit remarkable similarity among Sparse2Noise, Noise2Noise, and Noise2Inverse from the preceding sections, quantitative assessments with SNR reveal significant

differences among them for both samples. Specifically, paired *t*-test analysis indicates that Sparse2Noise significantly outperforms Noise2Noise ( $p < 0.001$  for hydrogel tissue scaffolds sample and  $p < 0.0001$  for rat's hindlimb sample with scaffolds implanted), and Noise2Noise outperforms Noise2Inverse ( $p < 0.0001$  for both samples).

Figure 9 presents additional quantitative analysis of grey value profiles, MTF, and NPS for hydrogel tissue scaffolds. PBI-HCT results from Sparse2Noise, Noise2Noise, and Noise2Inverse are compared with the original phase-retrieval-only images, showing that Sparse2Noise slightly outperforms the other methods.

Table 2 provides a summary that integrates all the results of various comparisons, clearly outlining the findings and conclusions using different algorithms under different imaging conditions.

## 4. Discussions

This work mainly examined the performance of proposed algorithm, Sparse2Noise, for low-dose PBI-HCT imaging and compared the resulting image quality to that of low-dose PBI-CT imaging. Results exhibit high similarity using Sparse2Noise for low-





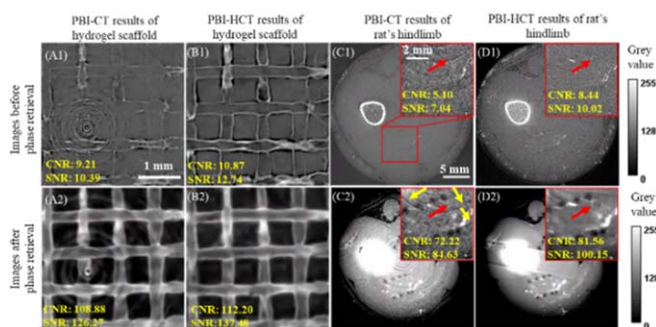


**Figure 7.** Comparison of low-dose PBI-CT and low-dose PBI-HCT using Noise2Inverse (before and after phase retrieval). (A1)-(A2) PBI-CT and (B1)-(B2) PBI-HCT results of hydrogel tissue scaffolds before and after phase retrieval. (C1)-(C2) PBI-CT and (D1)-(D2) PBI-HCT results of and rat's hindlimb sample with scaffolds implanted before and after phase retrieval. The red arrow indicates the degraded and swollen scaffolds and yellow arrows indicate the remaining ring artifacts.

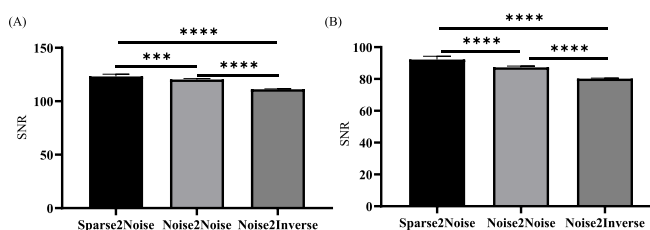


**Figure 8.** Corresponding statistical quantitative analysis of PBI-HCT results of (A) hydrogel tissue scaffolds at dose of 3.6 Gy and (B) rat's hindlimb sample with scaffolds implanted at dose of 1.0 Gy in terms of SNR. Paired t-test was utilized with \*\*\*\* indicating  $p < 0.001$ , and \*\*\*\*\* representing  $p < 0.0001$ .

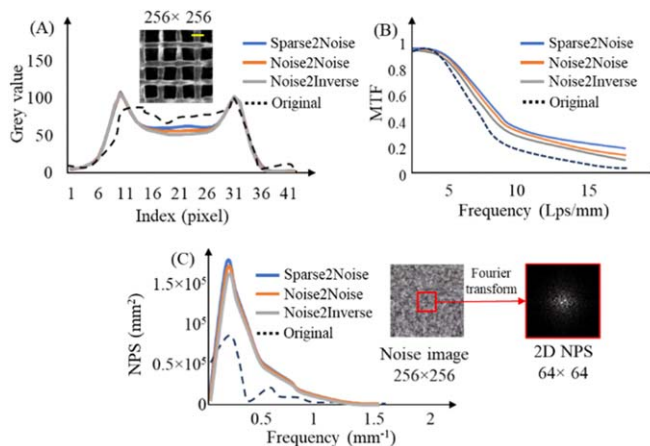


**Figure 9.** Quantitative analysis of PBI-HCT results (hydrogel tissue scaffolds) in terms of grey value profile, MTF, and NPS by using different algorithms, and compared with original images (i.e., phase-retrieval only).

In summary, the important contributions of this work rest on the following aspects. First, the proposed algorithm, i.e., Sparse2Noise, can effectively obtain high-quality results with less noise and reduced ring artifacts for PBI-HCT imaging. Second, compared to low-dose PBI-CT scanning, low-dose PBI-HCT scanning mode can obtain high image quality with lower radiation dose using Sparse2Noise. Besides, such helical scanning mode also enhances the performance of existing low-dose state-of-the-art to obtain higher image quality. Third, this study conducted a

comprehensive comparison of image quality using realistic low-dose PBI-CT and PBI-HCT data, highlighting the practical applications of various algorithms and their significance in real-world scenarios.

It is worth noting that Sparse2Noise for low-dose PBI-HCT imaging may encounter limitations in certain applications. Particularly, PBI-HCT imaging entails additional vertical movements, and mechanical accuracy is crucial to ensure precise alignment during separate scanning sessions, ensuring that the projections of samples are accurately matched in position.

**Table 2.** Experimental results summary of using different algorithms under different imaging conditions.

Algorithm	Input	target	Experimental findings
Sparse2Noise	Normal-flux sparse-view	Low-flux full-view	The image quality, both before and after phase retrieval, in terms of SNR and CNR, is comparable between PBI-CT and PBI-HCT for both low-density samples, i.e., hydrogel tissue scaffolds and the rat's hindlimb with implanted scaffolds.
	Low-flux sparse-view		PBI-HCT demonstrated higher image quality for both samples compared to PBI-CT.
Noise2Noise	Low-flux full-view	Low-flux full-view	PBI-HCT demonstrated higher image quality for both samples compared to PBI-CT.
Noise2Inverse	Low-flux full-view	Complementary low-flux full-view	PBI-HCT demonstrated higher image quality for both samples compared to PBI-CT.
Sparse2Noise vs. Noise2Noise versus Noise2Inverse	—	—	At the same radiation dose level, PBI-HCT imaging shows that, compared to Noise2Noise and Noise2Inverse, Sparse2Noise exhibits a significantly higher SNR, making it the most suitable algorithm for low-dose PBI-HCT imaging.

Any deviation in position may potentially introduce blurring or artifacts at the boundaries of samples. This aspect becomes increasingly critical, particularly for PBI-HCT imaging at higher resolutions, where even minor discrepancies can lead to noticeable blurring or artifacts. Future research endeavors will continue to explore the influence of these factors and seek viable solutions to mitigate potential challenges in PBI-HCT imaging, ensuring the continued advancement and refinement of this imaging technique for various applications. Although for results of rat's hindlimb sample with scaffolds implanted, low-dose PBI-CT and PBI-HCT imaging fail to unveil more specific structural details, this limitation is attributed to the degradation and swelling of the scaffolds occurring after two days post-implantation.

The application of Sparse2Noise for PBI-HCT imaging has significantly enhanced the image quality at an acceptable radiation dose level. This improvement holds promising implications for substantial advancements in future live animal biomedical research, demonstrating the potential for leveraging advanced imaging techniques to gain deeper insights into tissue scaffolds behavior and structural changes over time.

## 5. Conclusions

This study demonstrates the effectiveness of using the proposed low-dose imaging techniques (i.e., Sparse2Noise) in PBI-HCT imaging, achieving significant image quality while maintaining acceptable dose levels. The improvements observed in the results obtained from PBI-HCT compared to PBI-CT are notably more pronounced and the application conditions of Sparse2Noise are looser. This improvement achieved through Sparse2Noise for PBI-HCT facilitates a further reduction in dose by 30%–36% compared to PBI-CT. At the same radiation dose level,

PBI-HCT imaging show that compared to Noise2Noise and Noise2Inverse, Sparse2Noise exhibits a significantly higher SNR, which indicates Sparse2Noise is the most suitable algorithm for low-dose PBI-HCT imaging in practical visualization applications. These findings not only emphasize the potential of low-dose PBI-HCT in current research work, but also lay a solid foundation for its future exploration and application in the field of *in vivo* imaging, with the potential to make breakthrough progress in biomedical research and clinical diagnosis.

## Acknowledgments

This study was supported by the Natural Sciences and Engineering Research Council of Canada (NSERC, No. RGPIN 06007-2019 and No. RGPIN 06396-2019). Experimental research described in this paper were performed at the Canadian Light Source, which is a national research facility supported by the Canada Foundation for Innovation (CFI), NSERC, National Research Council (NRC), Canadian Institutes of Health Research (CIHR), Government of Saskatchewan, and the University of Saskatchewan.

## Data availability statement

The data that support the findings of this study will be openly available following an embargo at the following URL/DOI: <https://github.com/Xiaoman896/Sparse2Noise>. Data will be available from 1 July 2024.

## ORCID iDs

Xiaoman Duan  <https://orcid.org/0000-0003-1221-1609>

Xiao Fan Ding  <https://orcid.org/0000-0002-2137-6002>



Xiongbiao Chen  <https://orcid.org/0000-0002-4716-549X>

Ning Zhu  <https://orcid.org/0000-0002-2633-9956>

## References

- Albers J, Wagner W L, Fiedler M O, Rothermel A, Wünnemann F, Di Lillo F, Dreossi D, Sodini N, Baratella E and Confalonieri M 2023 High resolution propagation-based lung imaging at clinically relevant x-ray dose levels *Sci. Rep.* **13** 4788
- Chen B, Christianson O, Wilson J M and Samei E 2014 Assessment of volumetric noise and resolution performance for linear and nonlinear CT reconstruction methods *Med. Phys.* **41** 071909
- Chen H, Zhang Y, Kalra M K, Lin F, Chen Y, Liao P, Zhou J and Wang G 2017 Low-dose CT with a residual encoder-decoder convolutional neural network *IEEE Trans. Med. Imaging* **36** 2524–35
- Chen X, Anvari-Yazdi A F, Duan X, Zimmerling A, Gharraei R, Sharma N, Sweilem S and Ning L 2023 Biomaterials/bioinks and extrusion bioprinting *Bioactive Materials* **28** 511–36
- Duan X, Ding X F, Li N, Wu F-X, Chen X and Zhu N 2023a Sparse2Noise: low-dose synchrotron x-ray tomography without high-quality reference data *Comput. Biol. Med.* **165** 107473
- Duan X, Li N, Chen X and Zhu N 2021 Characterization of tissue scaffolds using synchrotron radiation microcomputed tomography imaging *Tissue Eng. C* **27** 573–88
- Duan X, Li N, Cooper D M, Ding X F, Chen X and Zhu N 2023b Low-density tissue scaffold imaging by synchrotron radiation propagation-based imaging computed tomography with helical acquisition mode *J. Synchrotron Radiat.* **30** 417–29
- Faragó T, Gasilov S, Emslie I, Zuber M, Helfen L, Vogelgesang M and Baumbach T 2022 Tofu: a fast, versatile and user-friendly image processing toolkit for computed tomography *J. Synchrotron Radiat.* **29** 16–27
- Gasilov S, Webb M A, Panahifar A, Zhu N, Marinos O, Bond T, Cooper D M and Chapman D 2024 Hard x-ray imaging and tomography at the biomedical imaging and therapy beamlines of canadian light source *Synchrotron Radiation* **31** 1346–57
- Hasan A M, Mohebbian M R, Wahid K A and Babyn P 2020 Hybrid-collaborative Noise2Noise denoiser for low-dose CT images *IEEE Transactions on Radiation and Plasma Medical Sciences* **5** 235–44
- Hendriksen A A, Pelt D M and Batenburg K J 2020 Noise2inverse: self-supervised deep convolutional denoising for tomography *IEEE Transactions on Computational Imaging* **6** 1320–35
- Kang E, Min J and Ye J C 2017 A deep convolutional neural network using directional wavelets for low-dose x-ray CT reconstruction *Med. Phys.* **44** e360–75
- Lehtinen J, Munkberg J, Hasselgren J, Laine S, Karras T, Aittala M and Aila T 2018 Noise2Noise: learning image restoration without clean data arXiv:1803.04189
- Mohabatpour F, Duan X, Yazdanpanah Z, Tabil X L, Lobanova L, Zhu N, Papagerakis S, Chen X and Papagerakis P 2022 Bioprinting of alginate-carboxymethyl chitosan scaffolds for enamel tissue engineering *in vitro Biofabrication* **15** 015022
- Momose A 2020 X-ray phase imaging reaching clinical uses *Physica Med.* **79** 93–102
- Ning L et al 2021 Noninvasive three-dimensional *in situ* and *in vivo* characterization of bioprinted hydrogel scaffolds using the x-ray propagation-based imaging technique *ACS Appl. Mater. Interfaces* **13** 25611–23
- Paganin D, Mayo S C, Gureyev T E, Miller P R and Wilkins S W 2002 Simultaneous phase and amplitude extraction from a single defocused image of a homogeneous object *J. Microsc.* **206** 33–40
- Pelt D M and Parkinson D Y 2018 Ring artifact reduction in synchrotron x-ray tomography through helical acquisition *Meas. Sci. Technol.* **29** 034002
- Preissner M, Murrie R, Pinar I, Werdiger F, Carnibella R, Zosky G, Fouras A and Dubsky S 2018 High resolution propagation-based imaging system for *in vivo* dynamic computed tomography of lungs in small animals *Physics in Medicine & Biology* **63** 08NT3
- Samei E, Bakalyar D, Boedeker K L, Brady S, Fan J, Leng S, Myers K J, Popescu L M, Ramirez Giraldo J C and Ranallo F 2019 Performance evaluation of computed tomography systems: summary of AAPM task group 233 *Med. Phys.* **46** e735–56
- Shan H, Padole A, Homayounieh F, Kruger U, Khara R D, Nitiwarangkul C, Kalra M K and Wang G 2019 Competitive performance of a modularized deep neural network compared to commercial algorithms for low-dose CT image reconstruction *Nature Machine Intelligence* **1** 269–76
- Shan H, Zhang Y, Yang Q, Kruger U, Kalra M K, Sun L, Cong W and Wang G 2018 3D convolutional encoder-decoder network for low-dose CT via transfer learning from a 2D trained network *IEEE Transactions on Medical Imaging* **37** 1522–34
- Taba S T, Baran P, Lewis S, Heard R, Pacile S, Nesterets Y I, Mayo S C, Dullin C, Dreossi D and Arfelli F 2019 Toward improving breast cancer imaging: radiological assessment of propagation-based phase-contrast CT technology *Acad. Radiol.* **26** e79–89
- Tavakoli Taba S, Baran P, Nesterets Y I, Pacile S, Wienbeck S, Dullin C, Pavlov K, Maksimenko A, Lockie D and Mayo S C 2020 Comparison of propagation-based CT using synchrotron radiation and conventional cone-beam CT for breast imaging *European Radiology* **30** 2740–50
- Wang G, Ye J C and De Man B 2020 Deep learning for tomographic image reconstruction *Nature Machine Intelligence* **2** 737–48
- Wu D, Gong K, Kim K, Li X and Li Q 2019 Consensus Neural Network for Medical Imaging Denoising with Only Noisy Training Samples *Medical Image Computing and Computer Assisted Intervention – MICCAI 2019* 11767 (Springer) 741–9
- Wysokinski T W, Chapman D, Adams G, Renier M, Suortti P and Thomlinson W 2007 Beamlines of the biomedical imaging and therapy facility at the Canadian light source: I *Nucl. Instrum. Methods Phys. Res., Sect. A* **582** 73–6
- Yuan N, Zhou J and Qi J 2020 Half2Half: deep neural network based CT image denoising without independent reference data *Phys. Med. Biol.* **65** 215020
- Zeller-Plumhoff B, Mead J L, Tan D, Roose T, Clough G F, Boardman R P and Schneider P 2017 Soft tissue 3D imaging in the lab through optimised propagation-based phase contrast computed tomography *Opt. Express* **25** 33451–68
- Zhang Y, Noack M A, Vagovic P, Fezzaa K, Garcia-Moreno F, Ritschel T and Villanueva-Perez P 2021 PhaseGAN: a deep-learning phase-retrieval approach for unpaired datasets *Opt. Express* **29** 19593–604